

Apparent Fracture in Polymeric Fluids under Step Shear

Okpeafoh S. Agimelen¹ and Peter D. Olmsted¹

¹*Soft Matter Physics Group, School of Physics and Astronomy,
University of Leeds, Leeds, LS2 9JT, United Kingdom*

(Dated: June 1, 2022)

Recent step strain experiments in well-entangled polymeric liquids demonstrated a bulk fracture-like phenomenon. This was taken, in these experiments, to signify the invalidity of the Doi-Edwards (DE) tube model. We have investigated this phenomenon using the Rolie-Poly equation, which approximates a successful version of the DE theory, and we find close quantitative agreement with the experiments, as well as with the proposal by Marrucci and Grizzuti in 1983 that entangled polymer liquids possess an elastic instability. The fracture is a transient manifestation of this elastic instability that relies on the amplification of spatially inhomogeneous fluctuations. It resembles spinodal decomposition, with strain playing the role of the conserved quantity.

PACS numbers: 47.50.Cd, 47.20.Gv, 47.50.Gj, 83.60.Wc

Keywords: entanglements, tube model, melt fracture, flow instability

Introduction—Entangled polymers are ubiquitous in the plastics industry, and control of their processing is vital for producing well-tailored materials [1]. The motion of an entangled polymer molecule is restricted to a tube-like region due to the constraints imposed by surrounding chains. The theory for this, due to Doi and Edwards (DE)[2], predicts a maximum in the shear stress T_{xy} as a function of shear rate [Fig. 1(a)], at a shear rate $\dot{\gamma}$ roughly equal to the reciprocal of the time τ_d for a polymer to diffuse along its tube (reptation time). This non-monotonic constitutive behaviour indicates instability, which can lead to inhomogeneous flows and shear banding [3]. This constitutive instability was widely implicated [4] in the spurt effect [5], responsible for instabilities in industrial processes; however, spurt is now usually attributed to wall slip [6]. In rapid startup flow the DE theory also predicts the rubber elastic behaviour of a stress overshoot [2, 7].

Banding was not inferred in early shearing experiments on polymer melts [8], and subsequently the mechanisms of chain stretch and convected constraint release (CCR) – chain relaxation due to the release of entanglement constraints – were incorporated into the DE theory [9]; CCR can restore stable constitutive behavior. However, new observations of shear banding in polymer solutions [10] seem to validate the DE instability [7, 11], and it remains unknown how active CCR is.

Our motivation is a surprising observation by Boukany *et al.* in step strain experiments (using flat plates) in poly(styrene-butadiene) melts with $Z \approx 53 - 160$ chain entanglements and strains $\gamma_0 \gtrsim 2$ [12], at very fast shear rates. After the step they observed homogeneous relaxation for a short time, after which the stress relaxed more rapidly and the material split into two layers moving in opposite directions, separated by a thin [$\lesssim 40 \mu\text{m}$] ‘fracture’ layer [Fig. 1 of [12]]. They claim that the tube model cannot describe this behaviour [7, 11]. A similar observation was reported in poly(ethylene oxide) melts [13]. However, long ago Marrucci and Grizzuti (MG) showed that the DE theory predicts non-uniform elastic

response for large enough rapid step strains [7], which could explain the anomalously fast stress relaxation of some melts subjected to step strains [14, 15]. Here we show how fracture follows from the elastic nature of the DE instability [7].

Model—We separate the total stress tensor \mathbf{T} into contributions from the polymer and a Newtonian solvent,

$$\mathbf{T} = G\mathbf{W} + \eta(\boldsymbol{\kappa} + \boldsymbol{\kappa}^T) - p\mathbf{I}, \quad (1)$$

where G is the plateau modulus, η is the solvent viscosity, the pressure p maintains incompressibility, \mathbf{I} is the identity tensor and $\kappa_{\alpha\beta} \equiv \partial v_\alpha / \partial r_\beta$. The fluid velocity \mathbf{v} obeys

$$\rho \frac{d\mathbf{v}}{dt} \equiv \rho \left[\frac{\partial}{\partial t} + (\mathbf{v} \cdot \nabla) \right] \mathbf{v} = \nabla \cdot \mathbf{T}, \quad (2)$$

where ρ is the fluid density. For very small Reynolds number, Eq. (2) reduces to $\nabla \cdot \mathbf{T} = 0$, which is used for the spatially resolved calculations.

The dimensionless polymeric conformation, or strain, tensor \mathbf{W} is assumed to obey the diffusive Rolie-Poly (RP) equation [7, 16],

$$\begin{aligned} \frac{d\mathbf{W}}{dt} = & \boldsymbol{\kappa} \cdot \mathbf{W} + \mathbf{W} \cdot \boldsymbol{\kappa}^T - \frac{1}{\tau_d}(\mathbf{W} - \mathbf{I}) - \frac{2 \left(1 - \sqrt{\frac{3}{\text{Tr}\mathbf{W}}} \right)}{\tau_R} \\ & \times \left(\mathbf{W} + \beta \left(\frac{\text{Tr}\mathbf{W}}{3} \right)^\delta (\mathbf{W} - \mathbf{I}) \right) + \mathcal{D} \nabla^2 \mathbf{W}, \end{aligned} \quad (3)$$

which is a simplified form of the GLaMM model for linear polymers [17]. Here, \mathcal{D} is the stress diffusion constant, τ_d is the reptation time, and the Rouse time τ_R governs the relaxation of stretch $\text{Tr}(\mathbf{W})$. The parameter β quantifies convective constraint release (CCR); a large value of β corresponds to more CCR, which leads to monotonic (stable) behaviour of the shear stress. Following successful fits to experiments [16] we use $\delta = -0.5$.

Calculations—We consider two infinite flat plates of separation L where the top plate is free to move and the

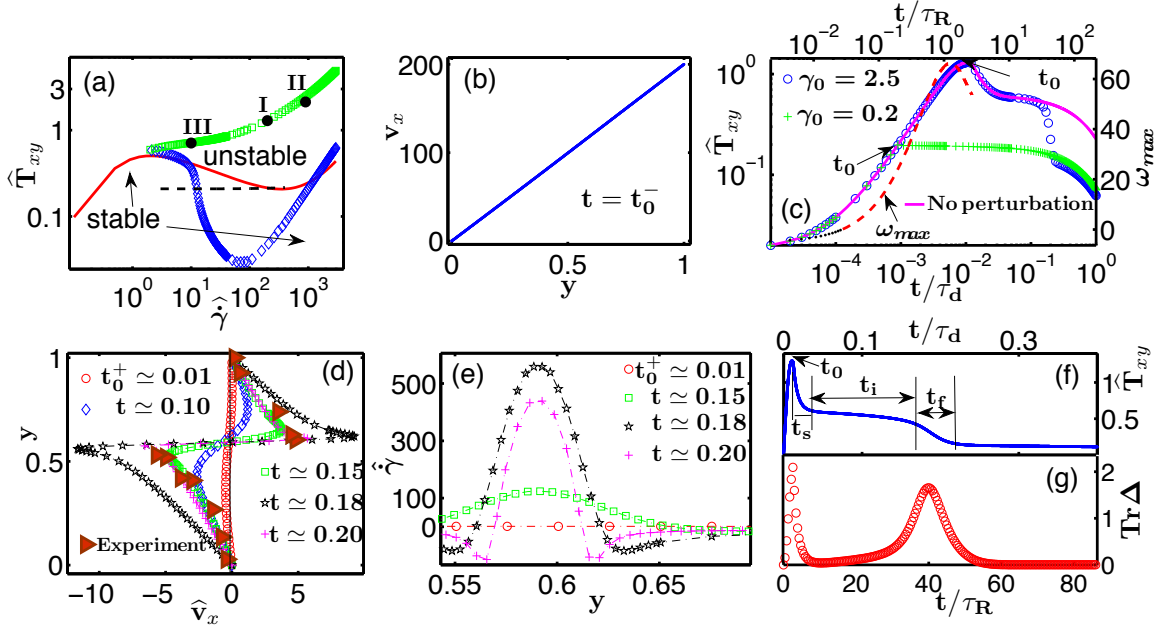


FIG. 1. (a) Constitutive (solid line) and steady state shear banding (black dashes) curves. The stress overshoot is indicated by green squares (\square); the homogenous base state becomes unstable ($\omega_{\max} > 0$) during startup at stresses given by the blue diamonds (\diamond). (b) Velocity profile at $t_0^- = 0.01249\tau_d$ (just before shear cessation) for $\langle \dot{\gamma} \rangle = 200$. (c) Stress relaxation for step strains $\gamma_0 = 0.2, 2.5$; the solid line is for $\gamma_0 = 2.5$ with no initial perturbation. The dot-dash line shows the evolution of the most unstable eigenvalue ω_{\max} , which becomes unstable ($\omega_{\max} > 0$) in the red (dashed) region. (d) Velocity profiles during fracture, with experimental data from [12] superposed. (e) Shear rate profiles, (f) stress relaxation, and (g) evolution of the maximum stretch in the gap $\text{Tr } \Delta^{\max}$. Parameters: $Z = 72$, $\tau_R = \tau_d/216$, $\langle \dot{\gamma} \rangle = 200$, $\gamma_0 = 2.5$, and $t_0 = 0.01250\tau_d$. Time t displayed in units of τ_d .

bottom plate is fixed. The flow direction is $\hat{\mathbf{x}}$ and the gradient direction is $\hat{\mathbf{y}}$ so that $\mathbf{v} = v_x(t, y)\hat{\mathbf{x}}$ and $\mathbf{W} = \mathbf{W}(t, y)$. The following dimensionless quantities are used: $\hat{\gamma} = \dot{\gamma}\tau_d$, $\hat{D} = D\tau_d/L^2$, $\epsilon = \eta/(G\tau_d)$, $\hat{\rho} = (\rho L^2)/(G\tau_d^2)$, $\hat{v} = (\tau_d v)/L$, and $\hat{t} = t/\tau_d$. The degree of entanglement Z determines the Rouse time via $\tau_R = \tau_d/(3Z)$ [16–18]. A desired average shear rate is imposed for a duration t_0 leading to a strain $\gamma_0 = \langle \dot{\gamma} \rangle t_0$.

The values $\tau_d = 310$ s and $Z = 55 - 100$ are consistent with the data in [12]; with $\eta \approx 1$ Pa s and $G \approx 7 \times 10^3$ Pa [19] we find $\epsilon \approx 10^{-7}$; for numerical stability we use $\epsilon = 10^{-4}$. For $L = 1$ mm, $\rho \approx 10^3$ kg m $^{-3}$ gives $\hat{\rho} \approx 10^{-10}$ and we use $\hat{D} = 10^{-5}$ [20]. Spatial derivatives are discretized using a semi implicit central finite difference scheme. For a timestep $\delta\hat{t} = 10^{-6}$ and 1000 spatial mesh points the maximum velocity in the fracture converges within 1 – 4% compared to $\delta\hat{t} = 10^{-5}$ or a mesh of 500. The time to fracture converges similarly.

We analyze stability using $\mathbf{u}(t) \equiv [\hat{\gamma}, \Delta_{xx}, \Delta_{xy}, \Delta_{yy}] = \bar{\mathbf{u}}(t) + \sum_k \delta \mathbf{u}_k(t) \exp(iky)$, where $\Delta \equiv \mathbf{W} - \mathbf{I}$. The homogeneous base state $\bar{\mathbf{u}}(t)$ is obtained by solving Eq. (3) for $D = 0$. Substituting $\mathbf{u}(t)$ into Eqs. (2, 3) and linearizing yields $\delta \dot{\mathbf{u}}_k = \mathbf{M}_k \cdot \delta \mathbf{u}_k$. We define ω_{\max} as the largest real part of the spectrum of eigenvalues of \mathbf{M}_k ; for $\omega_{\max} > 0$ the base state $\bar{\mathbf{u}}(t)$ is unstable with respect to small amplitude fluctuations [21, 22].

To capture the behaviour reported in [12], we con-

sider a fluid with non-monotonic constitutive behaviour, $\beta = 0$ [solid line in Fig. 1(a)], and use $Z = 72$ (consistent with [12]); this leads to shear banding and a stress plateau in steady state [dashes in Fig. 1(a)] [3]. We initialize Eq. (3) with random perturbations of the form $\delta \mathbf{u}(0, y) = \xi \sum_{n=1}^5 (A_n/n^2) \cos n\pi y$, $A_n \in [-1, 1]$, where ξ sets the overall scale of the perturbation. The penalty $1/n^2$ arises because high wavenumbers n should be suppressed by both spatial gradients in \mathbf{W} and by the slow dynamics of long wavelength velocity fluctuations that induce perturbations upon sample loading (for example). We use $\xi = 0.01$, consistent with the scale of typical thermal fluctuations in \mathbf{W} [23].

Perturbations can grow if the fluid becomes unstable [7, 22, 23]. Different random perturbations applied simultaneously to $\hat{\gamma}$ and Δ result in different velocity profiles after shear cessation at t_0 [24]. For 34% of 300 such simulations, the resulting velocity profiles were similar to the case reported in [12]. In all cases, the velocity profile was nearly homogeneous before shear cessation [Fig. 1(b)]. Using initial conditions (see later) that produce the experimentally observed velocity profile, we simulate examples reported in [12]: (I) Intermediate shear rates $\langle \dot{\gamma} \rangle \tau_R \approx 1$ and an applied strain γ_0 exceeding the strain γ_{ov} at which a stress overshoot occurs; (II) high shear rates $\langle \dot{\gamma} \rangle \tau_R > 1$ in the stretching regime and moderate strains $\gamma_0 \lesssim \gamma_{ov}$; and (III) lower shear rates $\langle \dot{\gamma} \rangle \tau_R < 1$

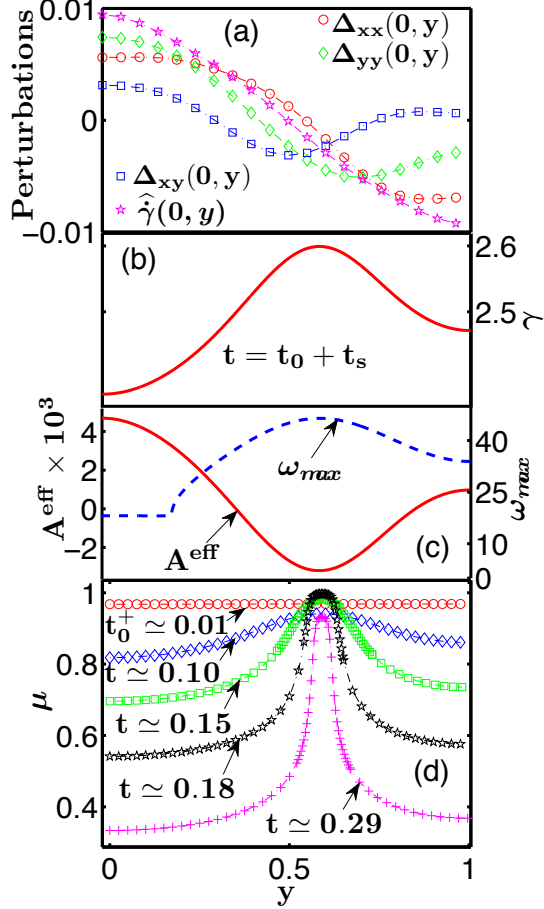


FIG. 2. Spatial profiles of (a) initial perturbation; (b) local strain; (c) effective modulus \mathcal{A}^{eff} as well as the unstable growth rate ω_{max} , after cessation of flow and subsequent stretch relaxation; (d) Evolution of unrelaxed polymer segments $\mu(y, t)$ during fracture development. [Parameters as in Fig. 1. Time t displayed in units of τ_d .]

and $\gamma_0 \lesssim \gamma_{ov}$. In all cases $\langle \dot{\gamma} \rangle \tau_d > 1$ and, as shown in Fig. 1(a), a homogeneous state is unstable before the cessation of flow at the imposed strain γ_0 .

Case I: $\langle \dot{\gamma} \rangle \tau_R \approx 1$ and $\gamma_0 > \gamma_{ov}$ — We impose $\langle \dot{\gamma} \rangle = 200$ ($\langle \dot{\gamma} \rangle \tau_R = 0.93$) for a strain $\gamma_0 = 2.5$. Immediately before cessation, at t_0^- , the velocity profile is imperceptibly inhomogeneous [Fig. 1(b)], while at t_0^+ the fluid stops with a slight inhomogeneity induced by the perturbation [Fig. 1(d)]. This perturbation slowly grows and localizes, leading to a ‘fracture’ plane at which the fluid shears very rapidly [Figs. 1(de)] and a sizeable stretch $\text{Tr } \Delta$ is induced [Fig. 1(g)] [24].

Some stress quickly relaxes due to stretch relaxation in a time $t_s \approx 7\tau_R$ [Fig. 1(cfg)] just after shear cessation; followed by an induction time $t_i \approx 30\tau_R$ that resembles homogenous reptation [blue circles in Figs. 1(c), 1(f)], before relaxing quickly in a time $t_f \approx 15\tau_R$ during the ‘fracture’ [Fig. 1(d)]. Thereafter it relaxes like a quiescent melt with a small initial strain $\gamma_0 = 0.2$ [Fig. 1(c)],

so that the stress released in the fracture corresponds to a plastic strain $\gamma_{\text{pl}} \approx 2.3$. Since the boundaries are fixed, positive shear strain within the slip layer is balanced by opposing recoil in the still-entangled outer regions [e.g. Fig. 1(e) for $t/\tau_d > 0.15$]. Without an initial perturbation only quiescent relaxation obtains [solid line of Fig. 1(c)]. The velocity profiles [Fig. 1(d)] are consistent with Fig. 1 of [12] (which has an induction time $t_i \approx 5\tau_R$).

Stability— Fig. 1(ac) shows that the material is unstable ($\omega_{\text{max}} > 0$) from well before the stress overshoot until shear cessation. To understand this instability, we turn to the Marrucci-Grizzuti (MG) observation that, for strain $\gamma_0 \gtrsim 2.1$ the elastic energy function $F(\gamma)$ for the DE model has a negative effective shear modulus $\mathcal{A} \equiv \partial^2 F / \partial \gamma^2 < 0$ [7], which heralds instability. Thus MG predicted elastic instability for a step strain, for

$$\mathcal{A}^{\text{eff}} \equiv \mu(t_0 + t_s) \left. \frac{\partial^2 F}{\partial \gamma} \right|_{\gamma_0} + [1 - \mu(t_0 + t_s)] \left. \frac{\partial^2 F}{\partial \gamma^2} \right|_0 < 0, \quad (4)$$

where $\mu(t)$ is the fraction of unrelaxed tube segments, whose value decreases when the chain segments lose their anisotropy and thus relax stress [2].

The anisotropy of the polymer conformation tensor \mathbf{W} defines $\mu \equiv |\lambda_1 - \lambda_2| / |\lambda_1 + \lambda_2|$, where λ_i are the eigenvalues of \mathbf{W} in the shear plane [25]. For a homogeneous state subjected to a step strain $\mu(t)$ relaxes homogeneously to zero. However, an inhomogeneous initial condition initiates instability and an inhomogeneous $\mu(y, t)$ [Fig. 2(d)], such that the fracture region experiences enhanced anisotropy and polymer stretch [Fig. 1(g)].

Fig. 2(bc) shows the spatial profiles for the strain and the effective shear modulus \mathcal{A}^{eff} after stretch relaxation [26]. The fracture region is most unstable, so that the initial perturbation [Fig. 2(a)] can localize strain. In the elastic limit $\dot{\gamma}\tau_d \gg 1$, $\mathcal{A}^{\text{eff}} \approx \partial T_{xy} / \partial \gamma = \dot{\gamma}^{-1} \partial T_{xy} / \partial t < 0$ [7, 11, 22, 23], which coincides with the stress overshoot. The unstable region predicted by the elastic limit coincides with the most unstable eigenvalue ω_{max} calculated from the full dynamics, which indicates instability before the stress overshoot is reached [e.g. Fig. 1(a)] because of the viscous contribution to the instability [22].

Conditions for fracture— A detailed study shows that perturbations in Δ_{xx} and Δ_{yy} induce fracture [24]. The step strain γ_0 advects the initial perturbation into a shear component of the polymer strain [e.g. $W_{xy}(y, t_0) \approx \gamma_0(1 + \Delta_{yy}(y, 0))$, which generates an inhomogeneous shear rate $\delta \dot{\gamma}(y, t_0^+) \approx -\gamma_0 \Delta_{yy}(y, 0) / \epsilon$ immediately after cessation of flow to maintain $\nabla \cdot \mathbf{T} \approx 0$]. Although general perturbations are complex [Fig. 2(a)] [24], if the perturbation leads to a local maximum in the polymeric strain γ , this then defines the position with most negative effective shear modulus $\mathcal{A}_{\text{eff}} < 0$ [Fig. 2(c)] [26], and thus the fracture position. This is born out by the dynamical calculation [Fig. 2(c)], which shows a critical unstable eigenvector dominated by the growth of Δ_{xx} and hence enhanced stretch in the flow direction [24].

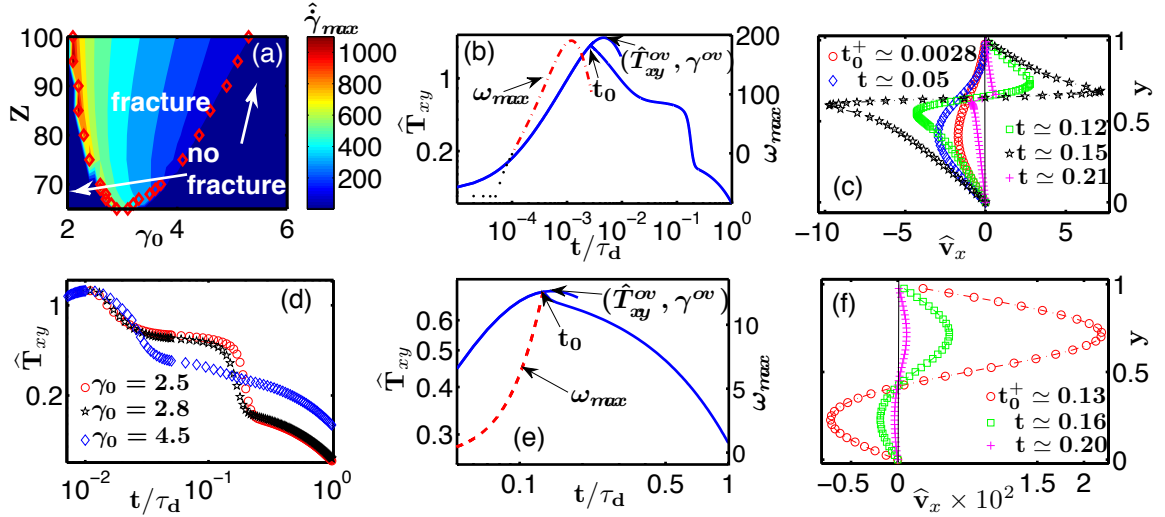


FIG. 3. (a) Values of Z and γ_0 required for fracture at fixed $\langle\dot{\gamma}\rangle$; contours show the maximum shear rates during fracture. (bc) Case II ($\langle\dot{\gamma}\rangle = 900$, $\langle\dot{\gamma}\rangle\tau_R = 4.2$, $\gamma_0 = 2.5$): (b) Stress relaxation and unstable growth rate ω_{\max} ; (c) velocity profiles during fracture. (d) Stress decay for three different imposed strains γ_0 . (ef) Case III ($\langle\dot{\gamma}\rangle = 10$, $\langle\dot{\gamma}\rangle\tau_R = 0.046$, $\gamma_0 = 1.3$): (e) Stress relaxation and ω_{\max} , and (f) velocity profiles. [All other parameters as in Fig. 1. Time t displayed in units of τ_d .]

The subsequent evolution resembles spinodal decomposition of a conserved quantity, since the total strain γ_0 is fixed. The strain in the most unstable region grows while that in the less unstable regions decreases, thus reducing their degree of instability. This leads to recoil and a sharpening of the deformation around the most unstable position, which can then fracture. The growing local maximum competes with reptation which relaxes the instability; hence for fracture to occur, the initial amplitude must be sufficiently large for it to localize and induce fracture before reptation relaxes the system. Fluids with large amounts of convected constraint release do not undergo fracture, because of the enhanced relaxation.

Character of Fracture—A larger strain leads to a less dramatic fracture [Fig. 3(ad)] because the total stress has passed the overshoot and decreased, hence releasing less stress into the fracture; however the molecular strain W_{xy} is larger, which leads to a faster growing instability. This is consistent with Fig. 8 of [12]. Alternatively, for a higher imposed strain rate the response is more dominated by stretching, which leaves less orientational stress and molecular strain after stretch relaxation so that fracture that takes longer to develop [22].

Further Comparisons:—We present two more comparisons with Ref. [12]. In **Case II** ($\langle\dot{\gamma}\rangle = 900$, $\langle\dot{\gamma}\rangle\tau_R = 4.2$), the shear rate is large but the strain $\gamma_0 = 2.5$ is slightly less than the overshoot strain γ_{ov} [Fig. 3(bc)]. The velocity profiles are similar to Case I, and consistent with Fig. 2 of [12]. Because the growth rate ω_{\max} is so rapid for the high shear rate, the smaller strain can effect the necessary large growth of the instability. In this case the induction time $t_i \simeq 30\tau_R$ is similar to that of Case I.

In **Case III** ($\langle\dot{\gamma}\rangle = 10$, $\langle\dot{\gamma}\rangle\tau_R = 0.046$) the shear rate

is relatively weak and the applied strain is just less than that of the stress overshoot $\gamma_0 \lesssim \gamma_{ov}$ [Fig. 3(ef)]. Here, the ‘fracture’ and recoil is much weaker than for the previous two cases, due to the small growth rate. Moreover, the stress does not show any distinguishable delay since the shear rate is so low that the fluid response is viscous dominated and its elastic nature does not show up clearly. The weak recoil agrees with Fig. 7 of [12].

Fig. 6 of [12] demonstrated that, for sub-overshoot strains, higher shear rates lead to longer induction times. However, our calculations predict that higher shear rates lead to longer induction times because of the faster growing instability [24]. We cannot explain this discrepancy.

Conclusion—Our calculations suggest that the fracture seen in recent step strain experiments on polymeric liquids [12, 13] results from the underlying elastic instability whose signature is stress overshoot during rapid startup [7, 27]. Once stretch degrees of freedom have relaxed, the deformed melt is elastically unstable so that small inhomogeneities grow into plastic strain (shear flow) in the most unstable regions. If this instability grows fast enough compared to reptation then a dramatic fracture can result for particular shapes of the initial disturbance. The perturbation’s shape and amplitude control whether fracture occurs.

In related work, Manning *et al.* studied a similar phenomenon in a shear-transformation-zone model of an amorphous solid [28], which can yield plastically via a fluid ‘shear band’ during startup of steady shear flow.

Boukany *et al.* suggested that the fracture demands new physics [12]. Certainly current tube models are incomplete [29]. However, our calculations are reasonable if the spatial features are smooth on length scales greater

than the tube diameter $a \simeq 3 - 4$ nm. For a gap of 1 mm, the fracture width $\delta x \simeq 0.05$ corresponds to a thickness of order $50 \mu\text{m}$, which is consistent with the dimension $\leq 40 \mu\text{m}$ reported in Ref. [12]. Higher experimental resolution will determine whether or not a continuum de-

scription of the tube model, as used here, is adequate.

Acknowledgments—This study was funded by the EU ITN DYNACOP. We thank Robyn Moorcroft, Suzanne Fielding, and Scott Milner for helpful advice.

Apparent Fracture in Polymeric Fluids under Step Shear: Supplementary Information

I. CALCULATIONS

A. Step-Strain Calculations for Different Initial Conditions

The starting point for the calculations is the diffusive Rolie-Poly (DRP) model, given by [7, 16]

$$\frac{d\mathbf{W}}{dt} = \boldsymbol{\kappa} \cdot \mathbf{W} + \mathbf{W} \cdot \boldsymbol{\kappa}^T - \frac{1}{\tau_d}(\mathbf{W} - \mathbf{I}) - \frac{2\left(1 - \sqrt{\frac{3}{\text{Tr}\mathbf{W}}}\right)}{\tau_R} \left(\mathbf{W} + \beta \left(\frac{\text{Tr}\mathbf{W}}{3} \right)^\delta (\mathbf{W} - \mathbf{I}) \right) + \mathcal{D}\nabla^2\mathbf{W}, \quad (5)$$

where \mathbf{W} is a polymer strain, $\kappa_{\alpha\beta} = \partial_\alpha v_\beta$, \mathbf{v} is the fluid velocity, τ_d and τ_R are the reptation and stretch relaxation times respectively, \mathbf{I} is the identity tensor, β measures the amount of convective constraint release in the system, δ is a fitting parameter and \mathcal{D} is stress diffusion constant.

We use the Cartesian coordinate system (for the case of simple shear flow where the fluid is placed between two infinite parallel plates of separation L) where $\hat{\mathbf{y}}$ is the velocity gradient direction and $\hat{\mathbf{x}}$ is the flow direction, $\mathbf{v} = v_x(t, y)\hat{\mathbf{x}}$ and $\mathbf{W} = \mathbf{W}(t, y)$. Substitution into Eq. 5 with $\mathbf{W} = \boldsymbol{\Delta} + \mathbf{I}$ gives

$$\begin{aligned} \frac{\partial \Delta_{xx}}{\partial t} &= 2\Delta_{xy}\hat{\gamma} - \Delta_{xx} - \frac{2\tau_d}{\tau_R}[1 - A][(\beta A + 1)\Delta_{xx} + 1] + \hat{\mathcal{D}}\frac{\partial^2 \Delta_{xx}}{\partial y^2} \\ \frac{\partial \Delta_{xy}}{\partial t} &= \hat{\gamma} + \hat{\gamma}\Delta_{yy} - \Delta_{xy} - \frac{2\tau_d}{\tau_R}[1 - A](\beta A + 1)\Delta_{xy} + \hat{\mathcal{D}}\frac{\partial^2 \Delta_{xy}}{\partial y^2} \\ \frac{\partial \Delta_{yy}}{\partial t} &= -\Delta_{yy} - \frac{2\tau_d}{\tau_R}[1 - A][(\beta A + 1)\Delta_{yy} + 1] + \hat{\mathcal{D}}\frac{\partial^2 \Delta_{yy}}{\partial y^2} \\ A &= \left(1 + \frac{\text{Tr}\boldsymbol{\Delta}}{3}\right)^{-1/2}, \end{aligned} \quad (6)$$

where $\hat{\gamma} = \dot{\gamma}\tau_d$, $\hat{\mathcal{D}} = \mathcal{D}\tau_d/L^2$. The total stress \mathbf{T} is then obtained from \mathbf{W} and a Newtonian solvent of viscosity η as

$$\mathbf{T} = G\mathbf{W} + \eta(\boldsymbol{\kappa} + \boldsymbol{\kappa}^T) - p\mathbf{I}, \quad (7)$$

where G is the plateau modulus and p is pressure, this gives the total shear stress as

$$T_{xy} = G\Delta_{xy} + \eta\dot{\gamma}. \quad (8)$$

To capture the behaviour reported in [12], we initialize Equations 6 with random perturbations of the form

$$\delta\mathbf{u}(0, y) = \xi \sum_{n=1}^5 (A_n/n^2) \cos(n\pi y), \quad (9)$$

where $\mathbf{u} \equiv [\hat{\gamma}, \Delta_{xx}, \Delta_{xy}, \Delta_{yy}]$. The amplitudes A_n are chosen randomly within $[-1, 1]$. The parameter $\xi = 0.01$ sets the overall scale of amplitude and a cosine series was chosen since it satisfies the boundary condition imposed on $\boldsymbol{\Delta}$. Using more modes does not change the resultant perturbation significantly due to the $1/n^2$ penalty on the amplitudes. Each component of \mathbf{u} is initially perturbed separately using different random perturbations. Then all components of \mathbf{u} are perturbed together with each quantity receiving a separate random perturbation. Sample results from these simulations are shown in Figs. 4, 5 and 6.

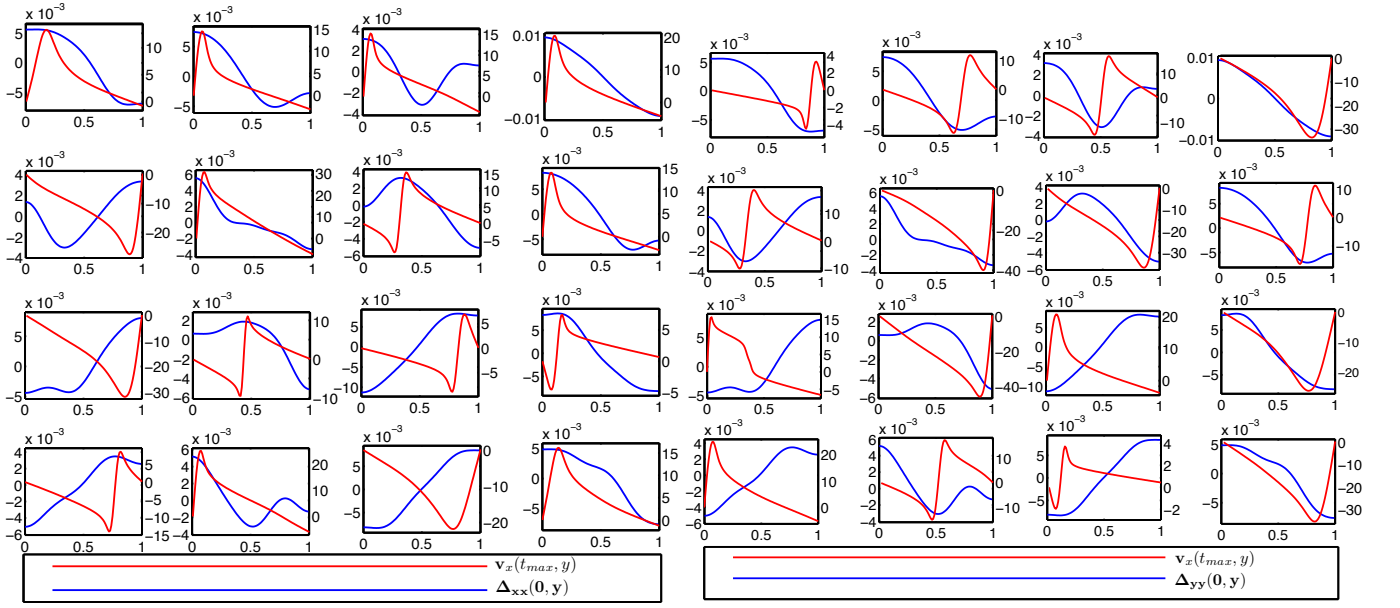


FIG. 4. Recoil or fracture for different random initial conditions upon perturbing Δ_{xx} (Left, about 31% fracture) and Δ_{yy} (Right, about 44% fracture). In all cases, the blue line is the perturbation and the red line is the velocity profile when both $\mu_{v\pm}$ reach their extrema together (for fracture) or $\mu_{v\pm}$ reach their extrema separately (for recoil without fracture). Left axis: perturbation; Right axis: velocity.

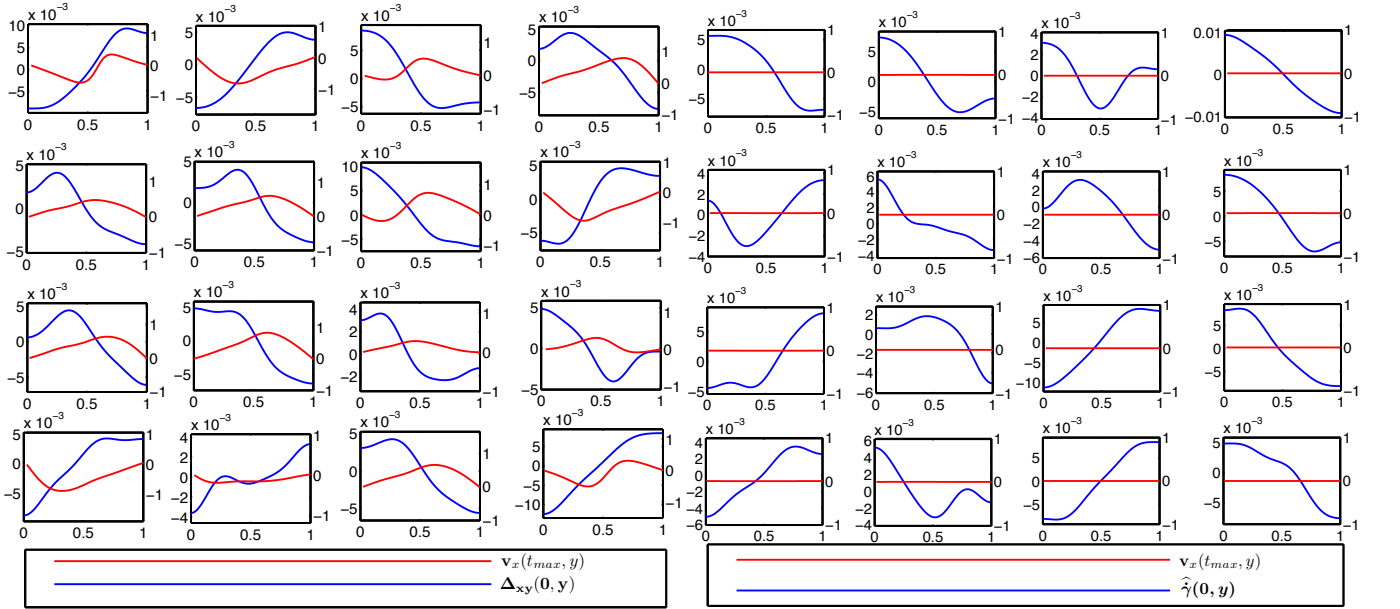


FIG. 5. Perturbation of Δ_{xy} (Left) and $\hat{\gamma}$ (Right). Only a weak recoil or a weak sign of fracture is seen in both cases. The blue and red lines have the same meaning as in Fig. 4. Left axis: perturbation; Right axis: velocity.

In all calculations reported here, the parameters were set as $Z = \tau_d/(3\tau_R) = 72$, $\hat{D} = 10^{-5}$, $\epsilon = \eta/(G\tau_d) = 10^{-4}$, $\beta = 0$ and for stability analysis, $\hat{\rho} = 10^{-10}$. To determine if fracture has occurred or not, consider the 'velocity moments' $\mu_{v\pm}$, defined by

$$\mu_{v\pm} = \sum_i v_i H(\pm v_i), \quad (10)$$

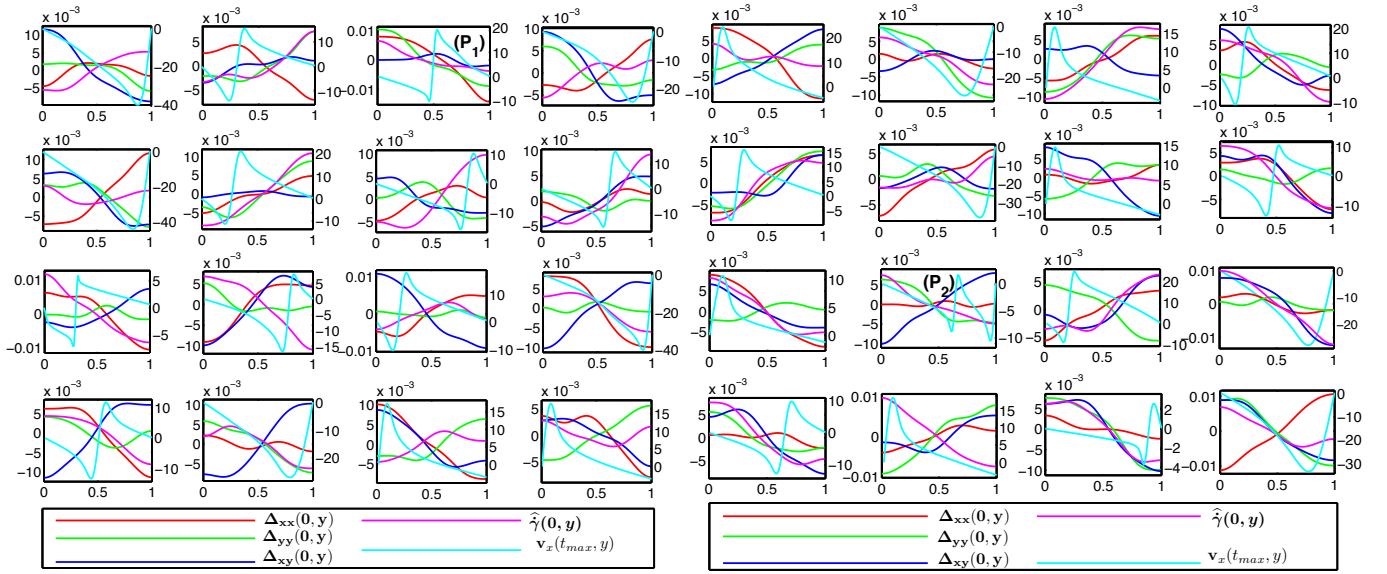


FIG. 6. Recoil or fracture upon perturbing all components, with each component receiving a separate random perturbation. Red line: perturbation to Δ_{xx} . Green line: perturbation to Δ_{yy} . Blue line: perturbation to Δ_{xy} . Magenta line: perturbation to $\dot{\gamma}$. Cyan line: recoil or fracture velocity profile v . Left axis: perturbation; Right axis: velocity. The left hand side shows about 56% fracture while the right hand side shows about 44% fracture (subfigure P_2 shows an example of two fracture planes). In all cases, the velocity profiles occur at the time specified in Fig. 4.

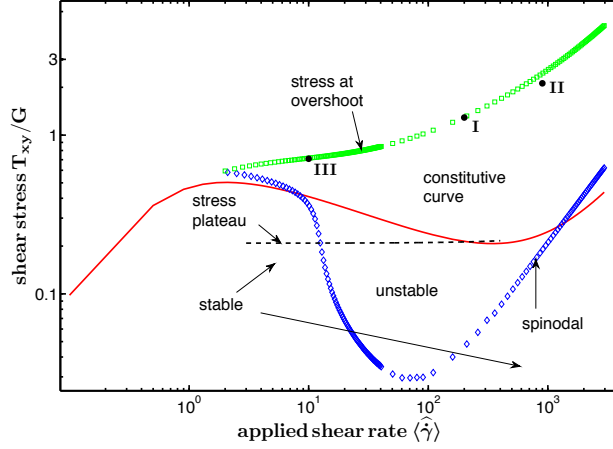


FIG. 7. Spinodal (shear stress at which the homogeneous state goes unstable), constitutive curve, stress plateau and the overshoot stress for the DRP model with $\beta = 0$, $Z = \tau_d/(3\tau_R) = 72$.

where the sum is over all spatial positions y_i and H is the Heaviside step function. If both positive moment μ_{v+} and negative moment μ_{v-} occur together at any time during stress relaxation after shear cessation, then fracture has occurred, otherwise there is no fracture. The velocity profiles shown in Figs. 4 to 6 occur at the time when both μ_{v+} and μ_{v-} reach their extrema for the case of fracture. When there is no fracture, the velocity profiles are shown when either μ_{v+} reaches its maximum or μ_{v-} reaches its minimum. When fracture occurs, the position of the fracture plane depends on the shape of the specific perturbation. The stress relaxation is independent of the position of the fracture plane, as in the experiments of [12] (section III A).

In about 34% of 300 simulations where Δ_{xx} , Δ_{yy} , Δ_{xy} and $\dot{\gamma}$ are all perturbed simultaneously, the resultant velocity profiles resemble the type reported in [12]. The calculations in the manuscript use a set of initial conditions that give a fracture with all quantities perturbed, such as subfigure P_1 in Fig. 6.

B. Linear stability analysis

Linear stability analysis is carried out following the approach described in [21, 29]. To this end the quantities are separated into a homogeneous part and a perturbation as

$$\mathbf{u}(t) = \bar{\mathbf{u}}(t) + \delta\mathbf{u}(t), \quad (11)$$

where $\bar{\mathbf{u}}(t) = [\hat{\gamma}, \bar{\Delta}_{xx}, \bar{\Delta}_{xy}, \bar{\Delta}_{yy}]$ is a homogeneous state obtained by solving

$$\begin{aligned} \partial_t \bar{\Delta}_{xx} &= 2\bar{\Delta}_{xy} \hat{\gamma} - \bar{\Delta}_{xx} - \frac{2\tau_d}{\tau_R} [1 - \bar{A}] [(\beta\bar{A} + 1) \bar{\Delta}_{xx} + 1] \\ \partial_t \bar{\Delta}_{xy} &= \hat{\gamma} + \hat{\gamma} \bar{\Delta}_{yy} - \bar{\Delta}_{xy} - \frac{2\tau_d}{\tau_R} [1 - \bar{A}] (\beta\bar{A} + 1) \bar{\Delta}_{xy} \\ \partial_t \bar{\Delta}_{yy} &= -\bar{\Delta}_{yy} - \frac{2\tau_d}{\tau_R} [1 - \bar{A}] [(\beta\bar{A} + 1) \bar{\Delta}_{yy} + 1] \\ \bar{A} &= \left(1 + \frac{\text{Tr} \bar{\Delta}}{3}\right)^{-1/2}. \end{aligned} \quad (12)$$

The perturbation $\delta\mathbf{u}(t, y)$ consists of fluctuations in the velocity gradient direction of the form

$$\delta\mathbf{u}(t, y) = \sum_k \delta\mathbf{u}_k(t) \exp(iky). \quad (13)$$

Substituting Eq. 8 into Eq. 6 and the momentum equation

$$\rho \frac{d\mathbf{v}}{dt} \equiv \rho \left[\frac{\partial}{\partial t} + (\mathbf{v} \cdot \nabla) \right] \mathbf{v} = \nabla \cdot \mathbf{T}, \quad (14)$$

where \mathbf{v} is the fluid velocity, ρ is the fluid density and \mathbf{T} is the total stress tensor, gives

$$\begin{aligned}
\partial_t \delta \Delta_{xx,k}(t) &= \left[\frac{\tau_d}{3\tau_R} \overline{\Delta}_{xx} (\beta - 1) \overline{A}^3 - 1 - \frac{\tau_d}{3\tau_R} \overline{A}^3 - 2 \frac{\tau_d}{\tau_R} [1 + (\beta - 1) \overline{A}] - \frac{2}{3} \beta \overline{\Delta}_{xx} \overline{A}^4 + 2\beta \overline{A}^2 \right. \\
&\quad \left. - k^2 \widehat{\mathcal{D}} \right] \delta \Delta_{xx,k}(t) \\
&\quad + 2\widehat{\gamma} \delta \Delta_{xy,k}(t) \\
&\quad + \left[(\beta - 1) \frac{\tau_d}{3\tau_R} \overline{\Delta}_{xx} \overline{A}^3 - \frac{\tau_d}{3\tau_R} \overline{A}^3 - \frac{2}{3} \beta \overline{\Delta}_{xx} \overline{A}^4 \right] \delta \Delta_{yy,k}(t) \\
&\quad + 2\overline{\Delta}_{xy} \delta \widehat{\gamma}_k(t) \\
\partial_t \delta \Delta_{xy,k}(t) &= \left[(\beta - 1) \frac{\tau_d}{3\tau_R} \overline{\Delta}_{xy} \overline{A}^3 - \frac{2}{3} \beta \frac{\tau_d}{\tau_R} \overline{A}^4 \overline{\Delta}_{xy} \right] \delta \Delta_{xx,k}(t) \\
&\quad + \left[2\beta \frac{\tau_d}{\tau_R} \overline{A}^2 - 1 - 2 \frac{\tau_d}{\tau_R} [1 + (\beta - 1) \overline{A}] - k^2 \widehat{\mathcal{D}} \right] \delta \Delta_{xy,k}(t) \\
&\quad + \left[\widehat{\gamma} + (\beta - 1) \frac{\tau_d}{3\tau_R} \overline{\Delta}_{xy} \overline{A}^3 - \frac{2}{3} \beta \frac{\tau_d}{\tau_R} \overline{\Delta}_{xy} \overline{A}^4 \right] \delta \Delta_{yy,k}(t) \\
&\quad + [1 + \overline{\Delta}_{yy}] \delta \widehat{\gamma}_k(t) \\
\partial_t \delta \Delta_{yy,k}(t) &= \left[(\beta - 1) \frac{\tau_d}{3\tau_R} \overline{\Delta}_{yy} \overline{A}^3 - \frac{\tau_d}{3\tau_R} \overline{A}^3 - \frac{2}{3} \beta \frac{\tau_d}{\tau_R} \overline{\Delta}_{yy} \overline{A}^4 \right] \delta \Delta_{xx,k}(t) \\
&\quad + \left[\frac{\tau_d}{3\tau_R} (\beta - 1) \overline{\Delta}_{yy} \overline{A}^3 - 1 - \frac{\tau_d}{3\tau_R} \overline{A}^3 - 2 \frac{\tau_d}{\tau_R} [1 + (\beta - 1) \overline{A}] - \frac{2}{3} \beta \frac{\tau_d}{\tau_R} \overline{\Delta}_{yy} \overline{A}^4 \right. \\
&\quad \left. + 2\beta \frac{\tau_d}{\tau_R} \overline{A}^2 - k^2 \widehat{\mathcal{D}} \right] \delta \Delta_{yy,k}(t) \\
\partial_t \delta \widehat{\gamma}_k(t) &= -\frac{k^2}{\widehat{\rho}} \delta \Delta_{xy,k}(t) - \frac{k^2 \epsilon}{\widehat{\rho}} \delta \widehat{\gamma}_k(t) \\
\epsilon &= \frac{\eta}{G\tau_d} \\
\widehat{\rho} &= \frac{\rho L^2}{G\tau_d^2},
\end{aligned} \tag{15}$$

where all nonlinear terms have been neglected. In the zero Reynolds number limit $\hat{\rho} \rightarrow 0$ this reduces to

$$\begin{aligned}
\partial_t \delta \Delta_{xx,k}(t) &= \left[\frac{\tau_d}{3\tau_R} \bar{\Delta}_{xx} (\beta - 1) \bar{A}^3 - 1 - \frac{\tau_d}{3\tau_R} \bar{A}^3 - 2 \frac{\tau_d}{\tau_R} [1 + (\beta - 1) \bar{A}] - \frac{2}{3} \beta \bar{\Delta}_{xx} \bar{A}^4 + 2\beta \bar{A}^2 \right. \\
&\quad \left. - k^2 \hat{\mathcal{D}} \right] \delta \Delta_{xx,k}(t) \\
&\quad + 2 \left[\hat{\gamma} - \frac{\bar{\Delta}_{xy}}{\epsilon} \right] \delta \Delta_{xy,k}(t) \\
&\quad + \left[(\beta - 1) \frac{\tau_d}{3\tau_R} \bar{\Delta}_{xx} \bar{A}^3 - \frac{\tau_d}{3\tau_R} \bar{A}^3 - \frac{2}{3} \beta \bar{\Delta}_{xx} \bar{A}^4 \right] \delta \Delta_{yy,k}(t) \\
\partial_t \delta \Delta_{xy,k}(t) &= \left[(\beta - 1) \frac{\tau_d}{3\tau_R} \bar{\Delta}_{xy} \bar{A}^3 - \frac{2}{3} \beta \frac{\tau_d}{\tau_R} \bar{A}^4 \bar{\Delta}_{xy} \right] \delta \Delta_{xx,k}(t) \\
&\quad + \left[2\beta \frac{\tau_d}{\tau_R} \bar{A}^2 - 1 - 2 \frac{\tau_d}{\tau_R} [1 + (\beta - 1) \bar{A}] - \frac{1 + \bar{\Delta}_{yy}}{\epsilon} - k^2 \hat{\mathcal{D}} \right] \delta \Delta_{xy,k}(t) \\
&\quad + \left[\hat{\gamma} + (\beta - 1) \frac{\tau_d}{3\tau_R} \bar{\Delta}_{xy} \bar{A}^3 - \frac{2}{3} \beta \frac{\tau_d}{\tau_R} \bar{\Delta}_{xy} \bar{A}^4 \right] \delta \Delta_{yy,k}(t) \\
\partial_t \delta \Delta_{yy,k}(t) &= \left[(\beta - 1) \frac{\tau_d}{3\tau_R} \bar{\Delta}_{yy} \bar{A}^3 - \frac{\tau_d}{3\tau_R} \bar{A}^3 - \frac{2}{3} \beta \frac{\tau_d}{\tau_R} \bar{\Delta}_{yy} \bar{A}^4 \right] \delta \Delta_{xx,k}(t) \\
&\quad + \left[\frac{\tau_d}{3\tau_R} (\beta - 1) \bar{\Delta}_{yy} \bar{A}^3 - 1 - \frac{\tau_d}{3\tau_R} \bar{A}^3 - 2 \frac{\tau_d}{\tau_R} [1 + (\beta - 1) \bar{A}] - \frac{2}{3} \beta \frac{\tau_d}{\tau_R} \bar{\Delta}_{yy} \bar{A}^4 \right. \\
&\quad \left. + 2\beta \frac{\tau_d}{\tau_R} \bar{A}^2 - k^2 \hat{\mathcal{D}} \right] \delta \Delta_{yy,k}(t)
\end{aligned} \tag{16}$$

This is a matrix equation of the form

$$\partial_t \delta \tilde{\mathbf{u}}(\mathbf{t}) = \mathbf{M}(t) \cdot \delta \tilde{\mathbf{u}}(\mathbf{t}), \tag{17}$$

where $\tilde{\mathbf{u}} = [\Delta_{xx}, \Delta_{xy}, \Delta_{yy}]$. Similar to the case described in [21], the eigenvalues of the stability matrix $\mathbf{M}(t)$ determine the (in)stability of the system: the system becomes unstable when the largest real part of an eigenvalue just becomes positive [21]. Hence the spinodal (the shear stress at which the fluid goes unstable during startup) for the system can be constructed as shown in Fig. 7. This region of instability matches the constitutive curve, similar to the situation reported in [21].

When the perturbation given in Eq. 9 is used to initialize the system, it induces some inhomogeneity in the system. Each point in space can then be considered as a base state and the stability of each of these base states to small amplitude fluctuations is also described by the stability matrix $\mathbf{M}(t)$. Hence the most unstable of these base states (which is the state whose eigenvalue has the largest real part) can be determined. This approach gives insight into the behaviour of the system when the quantities $\dot{\gamma}$, Δ_{xx} , Δ_{xy} and Δ_{yy} are perturbed separately. For 15 different initial conditions that give a fracture profile, the eigenvector $\tilde{\mathbf{v}}_m$ corresponding to the maximum real eigenvalue in space at the time of stretch relaxation is heavily dominated by the components Δ_{xx} and Δ_{yy} . The components of $\tilde{\mathbf{v}}_m$ for these different initial conditions are shown in Table I, where \tilde{v}_m^{xx} is the component in the flow direction, \tilde{v}_m^{xy} is the component in the shear direction and \tilde{v}_m^{yy} is the component in the velocity gradient direction. Hence perturbing the components $\dot{\gamma}$ and Δ_{xy} separately do not induce 'fracture' (as in Fig. 5) as compared with perturbing the components Δ_{xx} and Δ_{yy} separately at the same amplitude (as in Fig. 4).

C. Comparison with experiment

The calculations in the manuscript are based on the sample SBR 250K whose rheological properties are reported in Tables 1 and 2 of [12]. The rheological properties reported in Table 2 of [12] were said to have been measured from linear viscoelastic measurements (see section II B of [12]) but the Rouse times reported in Table 2 were estimated using $\tau_R^w = \tau/(M_w/M_e)$, where τ is the reptation time (section II B of [12]). However in our manuscript, the Rouse time is calculated using $\tau_R = \tau_d/(3Z)$ (as given in section I of [17]), where Z is the number of entanglements per chain. This then implies that the values of τ_R^w quoted in Table 2 of [12] are larger than the values of τ_R used in our manuscript by a factor of 3. We then present the data in [12] into different cases.

Case I: Intermediate Shear Rate, High Strain- Using $\langle \dot{\gamma} \rangle = 0.7 \text{ s}^{-1}$ given in Fig. 1a of [12] and $\tau_R^w = 4.1 \text{ s}$ quoted in Table 2 of [12] (for the sample SBR 250K) gives $\langle \dot{\gamma} \rangle \tau_R^w \simeq 2.9$. The sample SBR 250K (see Table 2 of [12])

TABLE I. Components of most unstable eigenvector $\tilde{\mathbf{v}}_m$ for 15 different initial conditions, for $\langle\dot{\gamma}\rangle = 200$, $\gamma_0 = 2.5$.

Initial Condition	\tilde{v}_m^{xx}	\tilde{v}_m^{xy}	\tilde{v}_m^{yy}
1	0.9657	-0.0115	-0.2594
2	0.9767	-0.0131	-0.2144
3	0.9678	-0.0118	-0.2516
4	0.9730	-0.0125	-0.2304
5	0.9632	-0.0112	-0.2687
6	0.9667	-0.0117	-0.2555
7	0.9678	-0.0118	-0.2513
8	0.9636	-0.0113	-0.2672
9	0.9739	-0.0127	-0.2266
10	0.9683	-0.0119	-0.2496
11	0.9675	-0.0118	-0.2524
12	0.9742	-0.0127	-0.2255
13	0.9666	-0.0116	-0.2562
14	0.9613	-0.0110	-0.2753
15	0.9596	-0.0109	-0.2812

has $M_w = 250000$ g/mol and $M_e = 3300$ g/mol giving $Z = M_w/M_e = 76$. Then using $Z = 76$, $\langle\dot{\gamma}\rangle\tau_d = 200$ and $\tau_d/\tau_R = 3Z$ gives $\langle\dot{\gamma}\rangle\tau_R \simeq 0.95$, which is comparable to the value of $\langle\dot{\gamma}\rangle\tau_R \simeq 1$ specified in case I of the manuscript, this is consistent with Fig. 1 of [12].

Case II: High Shear Rate, Low Strain– Similarly, $\langle\dot{\gamma}\rangle = 14$ s $^{-1}$ from [12] gives $\langle\dot{\gamma}\rangle\tau_R^w \simeq 57$, which is consistent with $\langle\dot{\gamma}\rangle\tau_R > 1$ given in case II of the manuscript and it agrees with Fig. 2 of [12].

Case III: Low Shear Rate, Low Strain– Again, $\langle\dot{\gamma}\rangle = 0.05$ s $^{-1}$ gives $\langle\dot{\gamma}\rangle\tau_R^w \simeq 0.2$, which is consistent with $\langle\dot{\gamma}\rangle\tau_R < 1$ given in case III of the manuscript, this has close agreement with Fig. 7 of [12].

The shear stresses at the time of shear cessation for the three cases I, II and III are indicated in Fig. 7. In case I, the shear stress had gone through the overshoot and it is beginning to decrease. In case two, the flow is switched off before the shear stress reaches the overshoot. Finally in case III, the flow is switched off just before the shear stress reaches the overshoot. Figure 1(c) of the manuscript shows a comparison of velocity profiles from the simulations and experimental data; the experimental data were obtained from V_{max} in Fig. 1c of [12], made dimensionless using $\hat{V}_{max} = V_{max}\tau/L$, where $\tau = 310$ s (from Table 2 of [12]) and $L = 0.7$ mm as given in section II of [12].

Induction time–To check the variation of the delay time after shear cessation before fracture sets in, we performed calculations at three different shear rates satisfying $\langle\dot{\gamma}\rangle\tau_R > 1$ (with τ_R fixed), similar to Fig. 6 of [12]. For $\langle\dot{\gamma}\rangle = 600$, $\langle\dot{\gamma}\rangle\tau_R \simeq 2.8$, $\langle\dot{\gamma}\rangle = 800$, $\langle\dot{\gamma}\rangle\tau_R \simeq 3.7$ and $\langle\dot{\gamma}\rangle = 1000$, $\langle\dot{\gamma}\rangle\tau_R \simeq 4.6$. In all cases, the applied strains are below the strain for overshoot at the applied shear rate as indicated by the lines l_1 and l_2 in Fig. 8(a). The overshoot stress is a linear function of the overshoot strain, as in Fig. 6(a) of [12]. Figures 8(bcd) show that, for varying strain and given shear rate, the higher plateau stress after stretch relaxation leads to a longer induction time. This characteristic is similar to the the situation in the inset of Fig. 6(b) of [12].

However, Figs. 8(e-f) show that for fixed strain and varying shear rate, the plateau stresses collapse, and the lower applied shear rate yielding a slightly longer induction time for $\gamma_0 = 2.2$. This can be linked to the faster growth rate ω_{max} observed for the very high shear rates, in which the viscous contribution to the instability dominates. However, this behaviour does *not* match that displayed in the inset of Fig. 6(b) of [12], in which the *higher* applied shear rate resulted in a larger induction time. We do not have an adequate explanation for these discrepancies.

II. MOVIES

The movies in <https://eudoxus.leeds.ac.uk/dynacop/FracturePage.html> illustrate the cases where the fluid undergoes fracture after shear cessation (**Fracture.avi**) and recoil without fracture (**Recoil.avi**) for case I. To achieve this, an initial condition of the form $\Delta_{xx}(0, y) = A(\cos(\pi y) + \phi \cos(2\pi y))$ is used to perturb the system. The shape and amplitude of this perturbation can be tuned to bring it close to one of the random perturbations which yields fracture-like behaviour when the component Δ_{xx} is perturbed. The amplitude is fixed at $A = 0.006$ while the

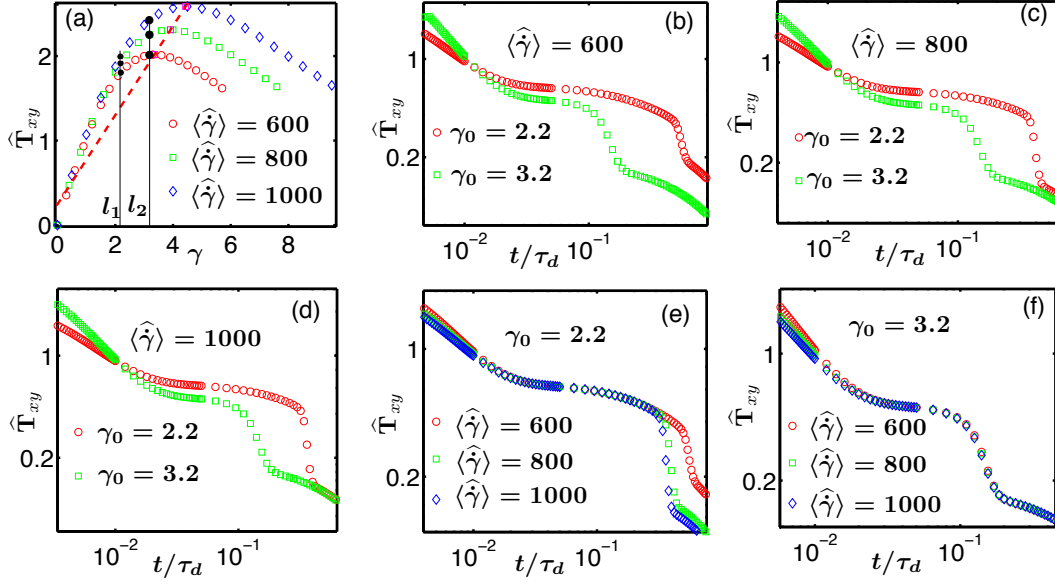


FIG. 8. (a) Shear stress versus strain at the three different applied shear rates indicated in the figure such that $\langle \dot{\gamma} \rangle \tau_R > 1$ in all cases, red circles: $\langle \dot{\gamma} \rangle \tau_R = 2.8$, green squares: $\langle \dot{\gamma} \rangle \tau_R = 3.7$ and blue diamonds: $\langle \dot{\gamma} \rangle \tau_R = 4.6$. The dashed line connects the strains for overshoot and their corresponding stresses for each applied shear rate, while the lines l_1 and l_2 indicate the applied strains $\gamma_0 = 2.2$ and $\gamma_0 = 3.2$ respectively. (b)-(f) Stress relaxation after step strains at different applied strains γ_0 and shear rates $\langle \dot{\gamma} \rangle$ indicated. Parameters as in Fig. 7.

parameter ϕ is varied to change the shape of the perturbation. The shapes of this perturbation for $\phi = 0.25$ and $\phi = 0.67$ are shown in Fig. 9(a).

For $\phi = 0.67$, the fluid fractures after shear cessation, the window on the left of **Fracture.avi** shows the fluid velocity from startup (with the upper plate fixed and the lower plate moving) to shear cessation and continues until the end of fracture. Before shear cessation, the fluid is seen to be moving to the left, after which the flow is switched off and the velocity vectors go to zero momentarily (except with a slight bulge due to the initial perturbation). The sizes of the velocity vectors before shear cessation are larger than their sizes after shear cessation by roughly one order of magnitude, hence to make the figure visible in the video, a rescaling of the figure window was carried out after shear cessation. The velocity profile v in the video on the left was made dimensionless using $\hat{v} = v\tau_d/L$. Then using $\tau_d = 310$ s and $L = 0.7$ mm (from [12]) gives the maximum size of velocity vectors v_{max} before shear cessation roughly equal to 0.45 mm s^{-1} and the maximum size after shear cessation is roughly equal to 0.02 mm s^{-1} . The velocity profile during fracture is shown in Fig. 9(b).

The figure window on the right of **Fracture.avi** shows the corresponding total shear stress T_{xy}/G from startup until the end of fracture. The total shear stress builds up quickly when the flow is switched on, and then just after the overshoot when the flow is switched off, the total shear stress goes through an initial quick relaxation during which the polymer chains relax stretch. It then enters a slow relaxation when reptation sets in. Although some reptation had already occurred during stretch relaxation, it becomes the dominant mechanism for stress relaxation after stretch relaxation. However, before reptation can completely relax the stress, the growing perturbation causes a sudden quick relaxation of stress. By this time the 'fracture plane' is fully developed and the fluid can be seen moving rapidly in two different directions on both sides of this plane. Finally when this rapid motion ceases, the stress resumes its slow relaxation and the material appears to have healed itself.

The case of $\phi = 0.25$, where the peak of the initial perturbation is not sharp enough as in Fig. 9(a), gives a completely different relaxation behaviour in the fluid as shown in **Recoil.avi**. The left window of that figure shows the fluid velocity from startup to shear cessation and beyond. Like in the case of $\phi = 0.67$, the top plate is fixed while the lower plate moves to the left. After shear cessation, the perturbation is seen to grow for a while but the fluid does not 'break' in two unlike in the case of $\phi = 0.67$. The growing perturbation loses the competition against the background reptation and hence the material heals itself and the fluid velocity vanishes after some time. Like in the case of $\phi = 0.67$, the figure window has been rescaled after shear cessation to make the velocity vectors visible. The maximum size of the velocity vectors before shear cessation is roughly equal to 0.45 mm s^{-1} while the maximum size after shear cessation is roughly equal to 0.006 mm s^{-1} . The recoil velocity for this case is shown in Fig. 9(b).

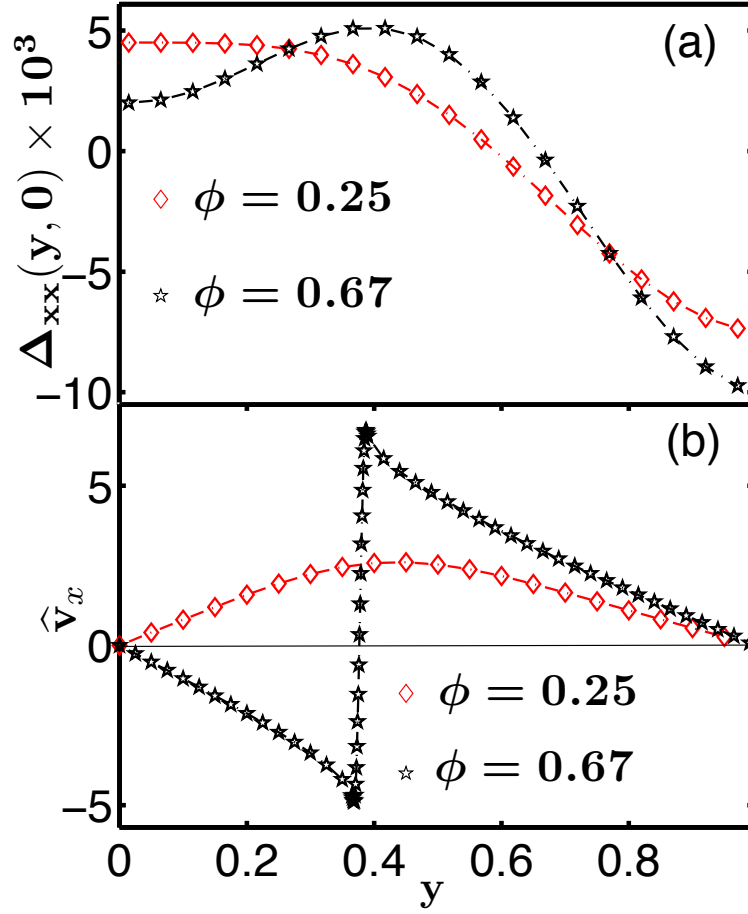


FIG. 9. (a) Initial perturbation for: $\phi = 0.25$ and $\phi = 0.67$, as shown in the movies `Recoil.avi` and `Fracture.avi`. (b) Recoil after shear cessation for $\phi = 0.25$ and fracture after shear cessation for $\phi = 0.67$. Parameters: $\beta = 0$, $Z = \tau_d/(3\tau_R) = 72$, $\langle \hat{\gamma} \rangle = 200$, and $\gamma_0 = 2.5$.

The right window of `Recoil.avi` shows the corresponding total shear stress for this case. It grows quickly from startup like the case of $\phi = 0.67$, then decays quickly during stretch relaxation and ends up with a slow relaxation due to reptation. The stress does not show any stage of rapid relaxation again since reptation is the dominant mechanism for stress relaxation in this case.

The movies were made with a mesh of 100 grid points to reduce the time taken to make them. The relevant parameters were set at $Z = 72$, $\hat{D} = 10^{-5}$, $\epsilon = 10^{-4}$, $\beta = 0$, $\gamma_0 = 2.5$ and $\langle \hat{\gamma} \rangle = 200$, which represent case I described in the manuscript.

-
- [1] T. C. B. McLeish, *Adv. Phys.* **51**, 1379 (2002); R. G. Larson, *Science* **333**, 1834 (2011).
 - [2] M. Doi and S. F. Edwards, *The Theory of Polymer Dynamics* (Oxford University Press, Oxford, 1989).
 - [3] N. A. Spenley, M. E. Cates, and T. C. B. McLeish, *Phys. Rev. Lett.* **71**, 939 (1993); P. D. Olmsted, *Rheol. Acta* **47**, 283 (2008); C.-Y. D. Lu, P. D. Olmsted, and R. C. Ball, *Phys. Rev. Lett.* **84**, 642 (2000).
 - [4] T. W. Huseby, *J. Rheol.* **10**, 181 (1966); Y. H. Lin, *ibid.* **29**, 605 (1985); T. C. B. McLeish and R. C. Ball, *J. Poly. Sci. B-Poly. Phys.* **24**, 1735 (1986); T. C. B. McLeish, *ibid.* **25**, 2253 (1987); D. S. Malkus, J. A. Nohel, and B. J. Plohr, *Siam J. Appl. Math.* **51**, 899 (1991); M. M. Denn, *Ann. Rev. Fluid Mech.* **22**, 13 (1990).
 - [5] G. V. Vinogradov, A. Y. Malkin, Y. G. Yanovskii, E. K. Borisenkova, B. V. Yarlykov, and G. V. Berezhnaya, *J. Polym. Sci.: Part A-2* **10**, 1061 (1972).
 - [6] F. J. Lim and W. R. Schowalter, *J. Rheology* **33**, 1359 (1989); S. Q. Wang, in *Polymers in Confined Environments*, *Adv. Poly. Sci.*, Vol. 138 (Springer, Berlin, 1999) pp. 227–275; M. M. Denn, *Ann. Rev. Fl. Mech.* **33**, 265 (2001).

- [7] G. Marrucci and N. Grizzuti, *J. Rheol.* **27**, 433 (1983); F. A. Morrison and R. G. Larson, *J. Polym. Sci.: B* **30**, 943 (1992); J. M. Adams and P. D. Olmsted, *Phys. Rev. Lett.* **102**, 067801 (2009); J. Cao and A. E. Likhtman, *ibid.* **108**, 028302 (2012).
- [8] E. V. Menezes and W. W. Graessley, *J. Polym. Sci.: B* **20**, 1817 (1982).
- [9] G. Ianniruberto and G. Marrucci, *J. Non-Newt. Fl. Mech.* **65**, 241 (1996); D. W. Mead and R. G. Larson, *Macromolecules* **31**, 7895 (1998).
- [10] Y. T. Hu, L. Wilen, A. Philips, and A. Lips, *J. Rheol.* **51**, 275 (2007); S. Ravindranath, S. Wang, M. Olechnowicz, and R. Quirk, *Macromolecules* **41**, 2663 (2008); P. Tapadia, S. Ravindranath, and S. Wang, *Phys. Rev. Lett.* **96**, 196001 (2006); Y. T. Hu, *J. Rheol.* **54**, 1307 (2010).
- [11] J. M. Adams and P. D. Olmsted, *Phys. Rev. Lett.* **103**, 219802 (2009); S.-Q. Wang, *ibid.* **103**, 219801 (2009).
- [12] P. E. Boukany, S.-Q. Wang, and X. Wang, *Macromolecules* **42**, 6261 (2009).
- [13] Y. Fang, G. Wang, N. Tian, X. Wang, X. Zhu, P. Lin, G. Ma, and L. Li, *J. Rheol.* **55**, 939 (2011).
- [14] K. Osaki, *Rheol. Acta* **32**, 429 (1993); S. Ravindranath and S.-Q. Wang, *Macromolecules* **40**, 8031 (2007); M. T. Islam, J. Sanchez-Reyes, and L. A. Archer, *J. Rheology* **45**, 61 (2001).
- [15] The relaxation of entangled polymers is characterized by the damping function $h(\gamma_0) \equiv G(\gamma_0, t)/G(t)$, where $G(\gamma_0, t) = \langle T_{r\theta} \rangle / \gamma_0$ [2]. The “Type C” anomaly occurs when $h(\gamma_0)$ falls significantly below the Doi-Edwards prediction [14], as happens due to the stress relaxation and fracture in Fig. 2.
- [16] A. E. Likhtman and R. S. Graham, *J. Non-Newt. Fl. Mech.* **114**, 1 (2003).
- [17] R. S. Graham, A. E. Likhtman, T. C. B. McLeish, and S. T. Milner, *J. Rheol.* **47**, 1171 (2003).
- [18] To scale $Z_0 \rightarrow Z$ at fixed material parameters requires rescaling $\epsilon \rightarrow \epsilon Z_0^3 / Z^3$ and $\hat{\rho} \rightarrow \hat{\rho} Z_0^6 / Z^6$.
- [19] P. Tapadia and S. Wang, *Phys. Rev. Lett.* **91**, 198301 (2003).
- [20] J. M. Adams, S. M. Fielding, and P. D. Olmsted, *J. Non-Newt. Fl. Mech.* **151**, 101 (2008).
- [21] S. M. Fielding and P. D. Olmsted, *Phys. Rev. Lett.* **90**, 224501 (2003); *Eur. Phys. J. E* **11**, 65 (2003).
- [22] R. L. Moorcroft and S. M. Fielding, “Criteria for shear banding in time-dependent flow of complex fluids,” (2012), [arXiv:1201.6259](https://arxiv.org/abs/1201.6259).
- [23] J. M. Adams, S. M. Fielding, and P. D. Olmsted, *J. Rheol.* **55**, 1007 (2011).
- [24] The Supplementary Information contains details about the stability calculation; and a study of the statistics of the effects of different initial conditions; movies are also available at <https://eudoxus.leeds.ac.uk/dynacop/FracturePage.html>.
- [25] The definition of unrelaxed segments $\mu(t)$ matches the linear relaxation function $G(t) \equiv T_{r\theta} / \gamma_0$ after a vanishing step strain $\gamma_0 \rightarrow 0$, as does the equivalent function used by Marrucci and Grizzuti for the DE model [7].
- [26] Following [7] we use the stored free energy due to the orientational distribution of tube segments, given within the independent alignment approximation by $F(\gamma) = \frac{1}{2} \int_0^1 \ln \left\{ \frac{1}{2} \left(1 + \gamma^2 x^2 + [(x^2 \gamma^2 - 1)^2 + 4\gamma^2 x^4]^{1/2} \right) \right\} dx$.
- [27] R. L. Moorcroft, M. E. Cates, and S. M. Fielding, *Phys. Rev. Lett.* **106**, 055502 (2011).
- [28] M. L. Manning, J. S. Langer, and J. M. Carlson, *Phys. Rev. E* **76**, 056106 (2007); M. L. Manning, E. G. Daub, J. S. Langer, and J. M. Carlson, **79**, 016110 (2009).
- [29] A. Likhtman, *J. Non-Newt. Fl. Mech.* **157**, 158 (2009); S. M. Fielding and P. D. Olmsted, *Phys. Rev. E* **68**, 036313 (2003).